Journal of Geography and Cartography (2021) Volume 4 Issue 2
doi:10.24294/jgc.v4i2.1309

ORIGINAL RESEARCH ARTICLE

Using of remote sensing and aeromagnetic data for predicting potential areas of hydrothermal mineral deposits in the Central Eastern Desert of Egypt

Mohamed Abdelkareem[1*], Abdelhady Akrby[1], Mousa Fakhry[1], Mohamed Mostafa[2]

[1] *Geology Department, South Valley University, Qena 83523, Egypt. E-mail: mohamed.abdelkareem@sci.svu.edu.eg*

[2] *Egyptian Mineral Resources Authority, Cairo, Egypt.*

ABSTRACT

This article explored mineral resources and their relation to structural settings in the Central Eastern Desert (CED) of Egypt. Integration of remote sensing (RS) with aeromagnetic (AMG) data was conducted to generate a mineral predictive map. Several image transformation and enhancement techniques were performed to Landsat Operational Land Imager (OLI) and Shuttle Radar Topography Mission (SRTM) data. Using band ratios and oriented principal component analysis (PCA) on OLI data allowed delineating hydrothermal alteration zones (HAZs) and highlighted structural discontinuity. Moreover, processing of the AMG using Standard Euler deconvolution and residual magnetic anomalies successfully revealed the subsurface structural features. Zones of hydrothermal alteration and surface/subsurface geologic structural density maps were combined through GIS technique. The results showed a mineral predictive map that ranked from very low to very high probability. Field validation allowed verifying the prepared map and revealed several mineralized sites including talc, talc-schist, gold mines and quartz veins associated with hematite. Overall, integration of RS and AMG data is a powerful technique in revealing areas of potential mineralization involved with hydrothermal processes.

Keywords: Remote Sensing; Aeromagnetic Data; Hydrothermal Alteration; Egypt

ARTICLE INFO

Article history:
Received 26 June 2021
Accepted 19 August 2021
Available online 24 August 2021

1. Introduction

Remote sensing technique commonly applied in reconnaissance studies. It represents an important way in deciphering several features such as geological, geomorphic, structural and mineral resources. NASA has launched several generations of unmanned Landsat satellites (1 to 8) that have acquired valuable RS data for mineral resources, structural features and land-use/cover information. Several studies used RS data for lithologic mapping[1–7], detecting HAZs[8–12], and characterizing the geologic and the geomorphic features[13,14]. Ratio images were performed for enhancing the spectral variations among the bands. This approach has been used in remote sensing to mark the spectral differences[15], to map lithology and HAZs[16]. This is because such transformation process can display a high contrast range of spectral characteristics than do individual bands.

Aeromagnetic data represent a significant factor in identifying subsurface structures based on the variation of the geomagnetic field, which results from the differences in the magnetite content of the associated rock units. Such geologic structures represented the conduit of

the mineral deposits associated with hydrothermal solutions. Therefore, integration of RS images and AMG data would complement the surface and subsurface view of the present study, where we can understand the surface/subsurface geologic structures, characterize the lithologic features, and highlight the probable areas of mineralization.

Several studies were conducted in the Central Eastern Desert (CED) of Egypt using RS data[17–22]. Landsat data were utilized for lithologic mapping and mineral exploration in arid regions[1–4,8,23]. O'Connor and McDonald (1988) used Landsat Thematic Mapper (TM) and applied color composite of band ratios 5/7, 5/1 and 4 in R, G, and B, respectively, to distinguish volcanic, serpentinite-mélange and late to post-tectonic molasse sedimentary units in the Central Eastern Desert of Egypt[18]. Sultan *et al.* (1988) integrated field and observations of Landsat data in the CED and revealed elongated NW-SE deformation associated with faulting and ductile shear zones, NW trending related to left-lateral faults, and some lithologic contacts related to faulting[19]. They related these features to the Najd fault systems and were not the results of obduction/accretion tectonics.

The main aim of the present study is to explore the optimum area of mineral resources based on combining surface/subsurface structural elements and zones of hydrothermal processes. So as to accomplish this objective the HAZs and areas of structural complexity will be delineated using SRTM, OLI and aeromagnetic data. Field and metalogenic data will validate the mineral predictive map.

2. Study area

The study area is situated in the eastern part of the CED of Egypt, extending between Longitudes 33o 52' 50" E and 34o 15' 00" E, and Latitudes 25o 54' 00" N and 26o 15' 00" N. It occupies about 11980 sq km. It represents an important part of the proposed "Golden Triangle" project area that extending in the CED of Egypt, between Qena, Safaga and Quseir (**Figure 1**). It occupies the area west of the Quseir city in the Red Sea that well known by G. Duwi (Quseir) area (**Figure 1**). Lithologically, the exposed rock units in the study area vary from Precambrian to recent. The Precambrian rock units are represented by igneous and metamorphic rocks. The eastern part of the basement exposure is overlain by younger sedimentary formation ranging in age from late Mesozoic to Quaternary.

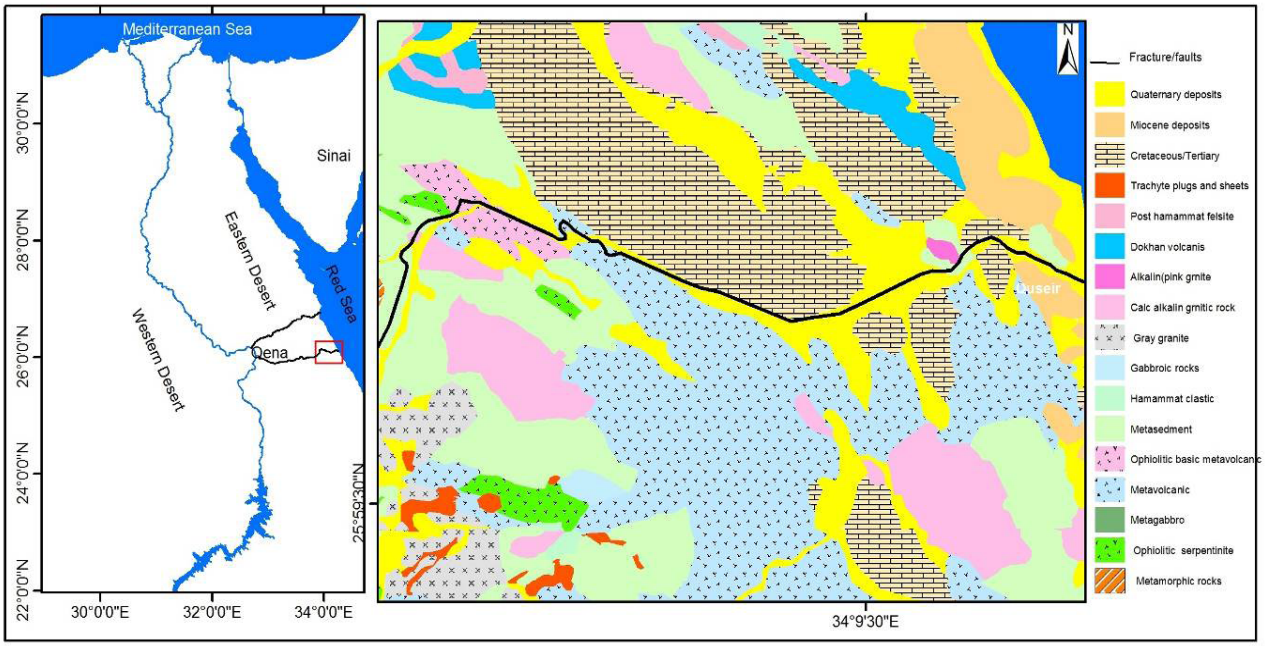

Figure 1. (a) Location map of the study area marked in red polygon nearness to the Red Sea zone. (b) Landsat ETM+ mosaic image showing the locality of the study area west of Quseir city and the accessible roads from Nile Valley to the Red Sea. (c) Geologic map of study (modified after Conoco, 1987)[24].

The study area occupied by Precambrian basement complex and Phanerozoic sedimentary rocks[25,26]. The basement complex, considered a part of the ANS which formed contemporaneously with the Late Proterozoic to Early Paleozoic time. During the Tertiary, the Arabian-Nubian Shield (ANS) was rifted apart by the Red Sea. The ANS of northeast Africa was cratonized during the late Pan-African Orogeny due to the collision of East and West Gondwana[27]. The basement complex in the ED of Egypt built up of island-arc/back-arc systems, consisting of metavolcanic, metasediments and associated ophiolitic rock assemblages[28,29]. These assemblages then, deformed and intruded by granitic masses of Syn- Late- and Post-tectonic during the Pan-African Orogeny.

3. Data used and methods

The available datasets such as a geological map, airborne total magnetic field survey, remote sensing, and field data were integrated in the present study using different spatial analysis techniques. Several studies were conducted to integrate aeromagnetic and RS data integration[7,30,31]. These studies have successfully displayed approaches to link the occurrence of mineral resources and understanding the surface and subsurface features.

3.1 Remote sensing data

In this article we utilized OLI data launched on February 11, 2013 from Vandenberg Air Force Base in California. OLI presents data from nine spectral bands (visible, near and shortwave infrared bands and two thermal long-wave bands). One image (path 174, raw 42) of Landsat data that acquired from USGS was processed using ENVI and ArcGIS software packages to extract the lithologic and HAZs.

Image transformation approaches like band ratios and PCA were utilized. In band ratios, dividing process of the digital numbers (DNs) of two spatially consistent bands are applied[5,32,33]. This technique clearly highlights the spectral variations of the mapped materials. Moreover, the PCA technique was performed. The statistical parameters are computed to characterize which component is significant based on the eigenvectors values to delineate the plausible area of hydrothermal alteration.

3.2 Aeromagnetic data

The utilized AMG data were compiled from the surveys that have been conducted in 1984 by the Western Geophysical Company of America (Aero Service Division), the Egyptian General Petroleum Corporation (EGPC) in conjunction with the Egyptian Geological Survey and Mining Authority (EGSMA).

The Aeromagnetic magnetic anomaly (TMI) data were processed to be reduced to the pole (RTP). This technique was done by subtracting the International Geomagnetic Reference Field (IGRF). The residual and Euler methods also were applied. Euler deconvolution technique applies potential field derivatives to reveal subsurface depth of a magnetic or gravity source[34]. It represents a valuable method for delineating contacts and depth estimation. The eminence of depth estimation depends on the selection of the structural index (SI) value and appropriate sampling of the data. It has become a tool to determine the source location of the potential field anomalies[35,36], and provides automatic estimates of source location and depth. To conduct this, the SI was applied to characterize many source types. The SI can be interpreted as the exponent in a power law expressing the decreasing of field strength versus distance from the source.

4. Results and discussion

4.1 Optical remote sensing data

Utilizing Landsat data allowed highlighting areas of hydrothermal alteration. This was based on the spectral signatures of the rock units. Utilizing band ratio composites 6/7, 6/5, 5 in R, G, and B, areas of HAZs that marked in yellow and pinkish colors were highlighted[37,38] (**Figure 2a, Figure 2b**).

The PCA of selected bands is applied in the selected study area. Selected bands of 2, 4, 5, and 6 of OLI sensor were developed to show iron oxide image (**Table 1**). The results showed that the eigenvalue represents 96.64% of total variance and the first

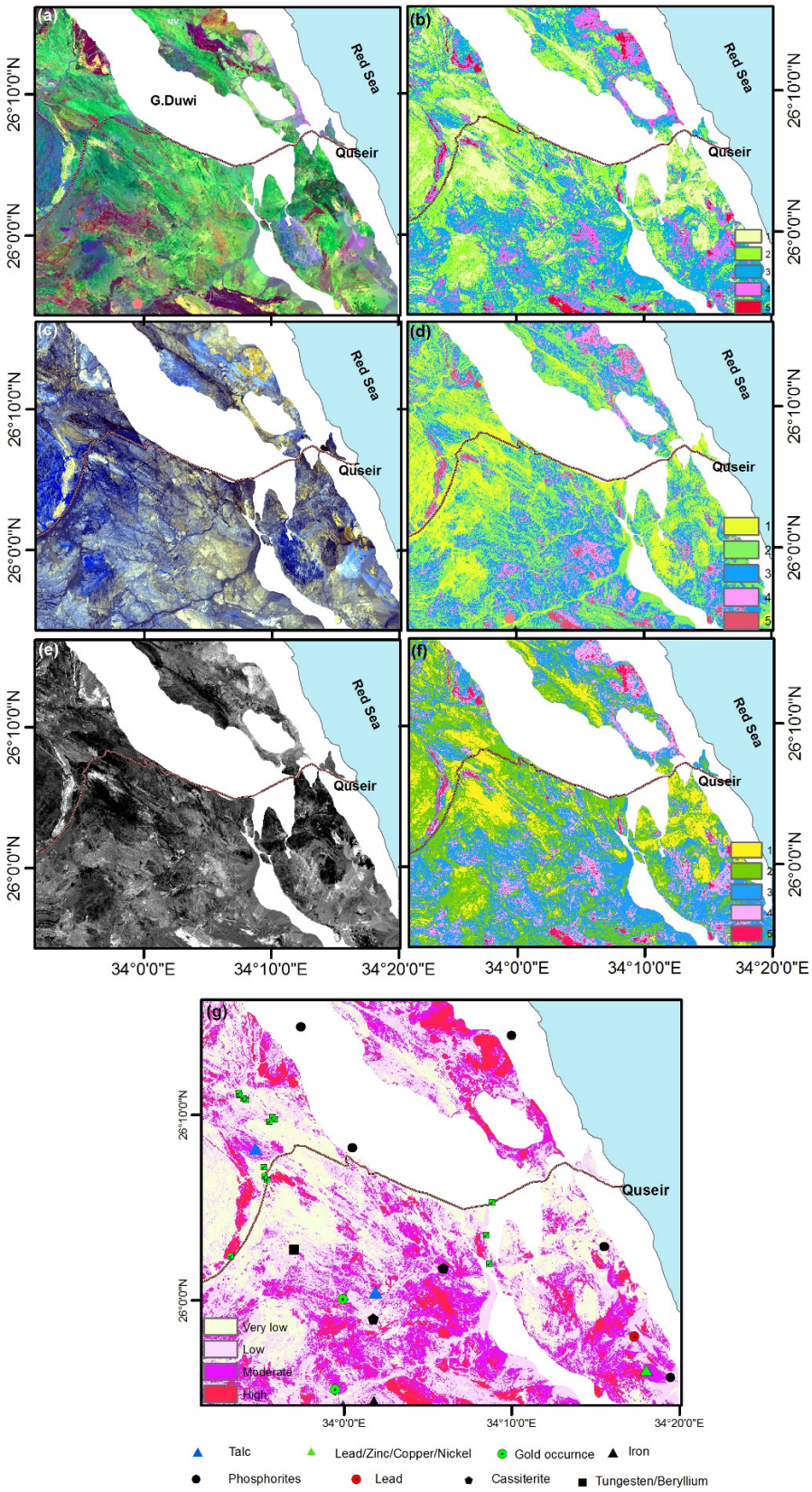

Figure 2. Alteration zones (a) band ratio 6/7, 6/5, 5; (b) classified band ratios of Ramadan *et al*.[40]; (c) Crosta technique, F, H+F, H in R, G, and B; (d) classified Crosta technique; (e) band ratios 6/7; (f) classified band ratios 6/7)alteration zones compiled from band ratios and PCA.; (g) alteration zone map of the study area**.**

component PC1 represents a positive loading from all bands. The PC4 displays positive loading from band 2 (0.70) versus band 4 (-0.66). Therefore, the PC4 was negated to display the iron-rich minerals in bright pixels.

In order to highlight areas of OH-bearing minerals, bands of 2, 5, 6, and 7 of Landsat-8 (image H) were used[10,39]. The results displayed that in PC3, there is a contrast between eigenvector loading from band 6 (-0.66) and band 7 (0.59). Therefore, the darkest pixels represent the OH-bearing minerals. After negation of the PC3, the hydrothermal altered areas appear in bright tone.

In order to generate Crosta's alteration image (**Figure 2c**), the F, H+F, H images are displayed in R, G, and B, respectively. This showed the suggested alteration zones in brighter whitish-yellowish hues. Higher DN defines the optimum areas of the alteration zones. The resulted map was classified into many classes depending on the grade of the alteration. Undesirable similar hues resulted from the sediments are masked by white polygon. Noteworthy, displaying band ratio 6/7 also highlighted the OH-bearing minerals (**Figure 2e, Figure 2f**) much more similar to Crosta technique. Accordingly, the HAZs are clearly highlighted in bright tone that graded into five zones (**Figure 2f**).

The extent of alteration zones is considered here for exploring areas of mineral resources which connected to hydrothermal activities. The Landsat data allowed highlighting the HAZs (**Figure 2g**). Combining data from band ratios and PCA well defined the rock alteration resulting from the hydrothermal activities. These zones can distinguish areas rich in hydroxyl and iron-oxide alterations. Therefore, this image was graded into five ranks after assigning weight factor for each class. The higher weight (numeric number) represents a higher grade of mineral favorability (**Figure 2g**).

4.2 Radar remote sensing for lineament extraction

Analysis of SRTM DEM (**Figure 3a**) revealed that the variations in topography range from 0 to 876 m (a.s.l). Moreover, it provided information on the geometry that was not identifiable by other RS techniques. The most elevated areas encountered in G. Duwi (elongated ridge trends NW–SE; ~550 m), G. Hamrawein (~650 m), G. Umm Himeiyir (~580 m), G. Murr (~715 m), and G. Umm Shagir (~600 m). The geological interpretation of the Landsat imagery and SRTM data (**Figure 3a**) revealed structural discontinuity that represented in lineaments. The results of lineaments analysis including density map (**Figure 3d**) and the distribution of lineaments using rose diagram reveal that the basement rocks (e.g. granites, metavolcanics, metasediments) and Cretacious/Tertiary sedimentary succession in the investigated area are highly fractured, while the area of sedimentary rocks displays less density. The lineaments density map also reveals discontinuous distribution on the area which revealing a major tectonics. Plotting lineaments on Rose diagram of Rock ware software packages (**Figure 3c**) reveals that the study areas are dominated by trends of N 30° W, and N 40° W, N 35° E, N 45° E; however, N-S and E-W respectively, according to decreasing of abundance. The NW-SE lineaments have longer and abundant in number than the NE-SW, N-S, and E-W trends.

5. Aeromagnetic data

5.1 Aeromagnetic anomalies

The study area reveals a magnetic anomaly ranging between -181.5 and 33.2 nT. The high magnetic anomalies, which characterized by short wavelengths, are observed in the southeastern, northwestern and western parts. However, the lowest magnetic anomalies (along wavelengths) are located in the southern part of the study area (**Figure 4a**). These anomalies are characteristic for the areas of the basement rocks outcrops and that covered by sedimentary cover, respectively. The sedimentary cover areas of Gabel Duwi area and its surroundings and the coastal area are manifested with the areas of low magnetic anomalies. The magnetic anomaly map revealed that the study area is structurally controlled and the predominant trends of the anomalies are NW-SE, NE – SW, N-S, and E-W.

The magnetic variation map (**Figure 4a**) was

Table 1. PCA of selected bands 2, 4, 5 and 6

Eigenvector	Band 2	Band 4	Band 5	Band 6	Eignvalue %
PC1	0.15022	0.441575	0.609239	0.641306	96.64965
PC2	0.221567	0.369174	0.481423	-0.763447	2.71183
PC3	0.660352	0.479502	-0.574698	0.061116	0.517105
PC4	0.701624	-0.66242	0.258423	0.046263	0.121419

Table 2. PCA of selected bands 2, 5, 6 and 7

Eigenvector	Band 2	Band 5	Band 6	Band 7	Eigenvalue %
PC1	-0.120062	-0.49843	-0.67361	-0.53236	97.5627
PC2	-0.2805	-0.75513	0.157252	0.571283	1.627296
PC3	0.425616	0.155359	-0.66236	0.596655	0.616379
PC4	0.851913	-0.3965	0.287758	-0.18502	0.193578

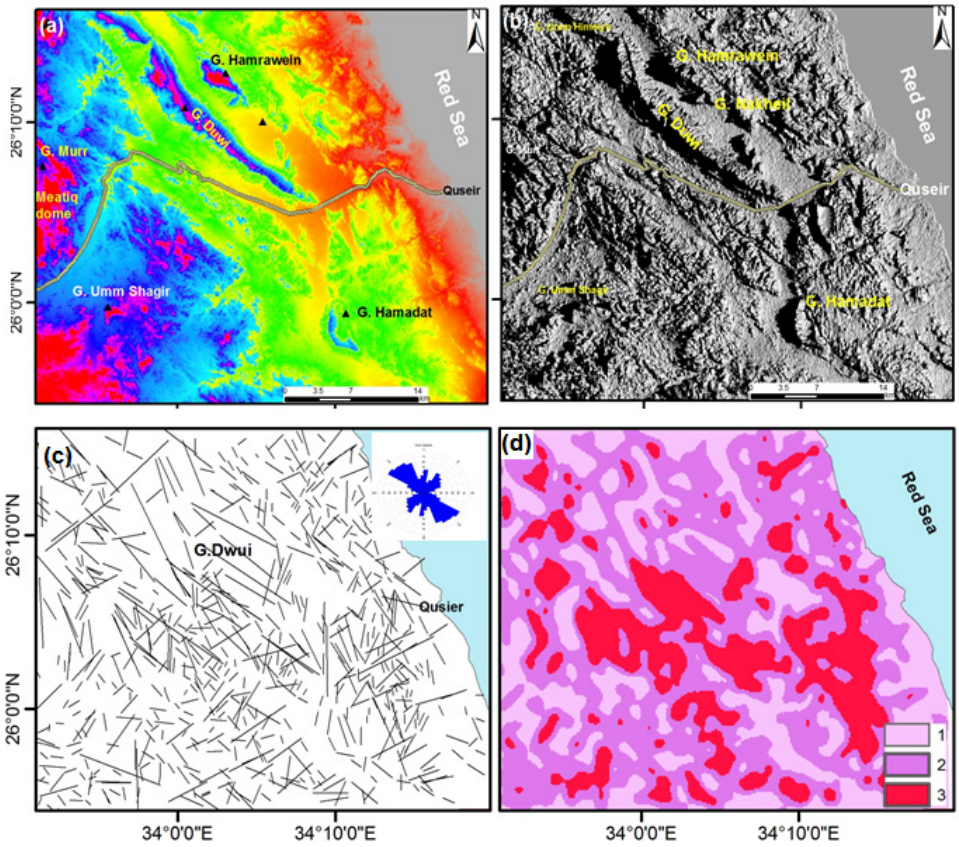

Figure 3. (a) SRTM-DEM m; (b) hill shade relief; (c) lineaments derived from remote sensing data; (d) lineament density of remote sensing data**.**

transformed into reduction to the pole (RTP) grid using the 2D – FFT (Fast Fourier Transform) filter (**Figure 4b**). The parameters which used for the transformation include an inclination of 39.5 and declination of 2, representing the mean values.

The resulted RTP map of the study area (**Figure 4b**) shows the presence of many magnetic zones with maximum amplitude values of about 115 nT. They are observed in southeastern and southwestern parts of the study area that associated with a metavolcanics, metasediments, metagabbros and younger granites above G. Umm Shagier, G. Muweilih, G. Umm Khurs and north G. Hamadat. Similar observations are detected in the western part related to metamorphic complexes of G. Umm Baanib and also in the northern part. The magnetic anomalies of this zone are defined by a broad high magnetic anomaly with an elongated to semicircular shape. These anomalies trend in the NE-SW, NW-SE, N-S and E-W directions. On the other hand, the magnetic anomalies with a low amplitude value of -228.95 nT are observed at the southwestern part of the study area and they are related to metasediments and Quaternary deposits above G. Umm Hombose. These areas also marked by the elongated shapes that trend in NE-SW and NW-SE directions.

5.2 Residual magnetic anomalies

In areas of basement exposures, the aeromagnetic anomalies reflect the magnetic mineral contents of the rock units[30]. Magnetic variations in areas of fracture/fault zones represent the favorable sites of mineralization. In the residual map, there are chains of small circular peaks magnetic anomaly closures, associated with volcanic and granitoid intrusions (**Figure 4c**). Porphyry deposits are often around the intrusive masses[41]. For example, tin (Sn) deposits most likely occur in the outer zone of the granitic body and tin also associated with magnetite mineralization. Therefore, these areas shown in **Figure 4c** reveal high grade of magnetic intensity. Many magmatic intrusions and quartz veins are involved with the hydrothermal activities. According to Rigol-Sanchez *et al.*[30], the high residual magnetic values pointed out zones of plausible ore-bearing buried anomalous bodies. Therefore, zones of elevated magnetic anomalies highlight areas of higher magnetic content. In addition to the aforementioned information, the image clearly highlighted the NE-SW zone that probably intersected and dislocated the NW-SE basin.

5.3 Euler deconvolution

The Euler deconvolution method was performed using the RTP grid with structural indexes of (0) and with a moving window of 10 x 10 and Euler solution was accepted on the criterion of errors 10%. The resulted map obtained in this case (**Figure 4d**) shows depth solutions ranges from 0 to 2000 m and most of these solutions are fall in the range of 0 to 500 m represented the shallow sources. These causative sources are extended in the NW-SE, NE-SW, and N-S.

5.4 Lineaments derived from aeromagnetic data

Subsurface linear structures identified in the study area from regional and residual magnetic maps (**Figure 5a** and **Figure 5b**) revealed lineations with trend directions in NW-SE, NE-SW, NNW-SSE, and NNE-SSW, with minor directions in ENE-WSW and WNW-ENE. Lineament density map obtained from sub-surface aeromagnetic data revealed the majority of elongated NW-SE zones and their intersected NE-SW trends (**Figure 5b**).

The lineaments that were deduced from aeromagnetic data are compiled from RS to produce an integrated lineament map (**Figure 6a**) which represents the major surface and sub-surface structures (faults/fractures). Analysis of lineament of both RS and AMG data revealing that the NW-SE and NE-SW lineaments are predominant trends in the present study. The extracted lineaments from these data were interpreted to density map (**Figure 6b**). This map revealed a high density of fracture/fault zones around Umm Had, Duwi area, Wadi Kareim, and in the middle section of the study area. Moreover, the density map reveals a predominant NW-SE trend that intersects by the NE-SW trend.

The detected linear trends have played a major

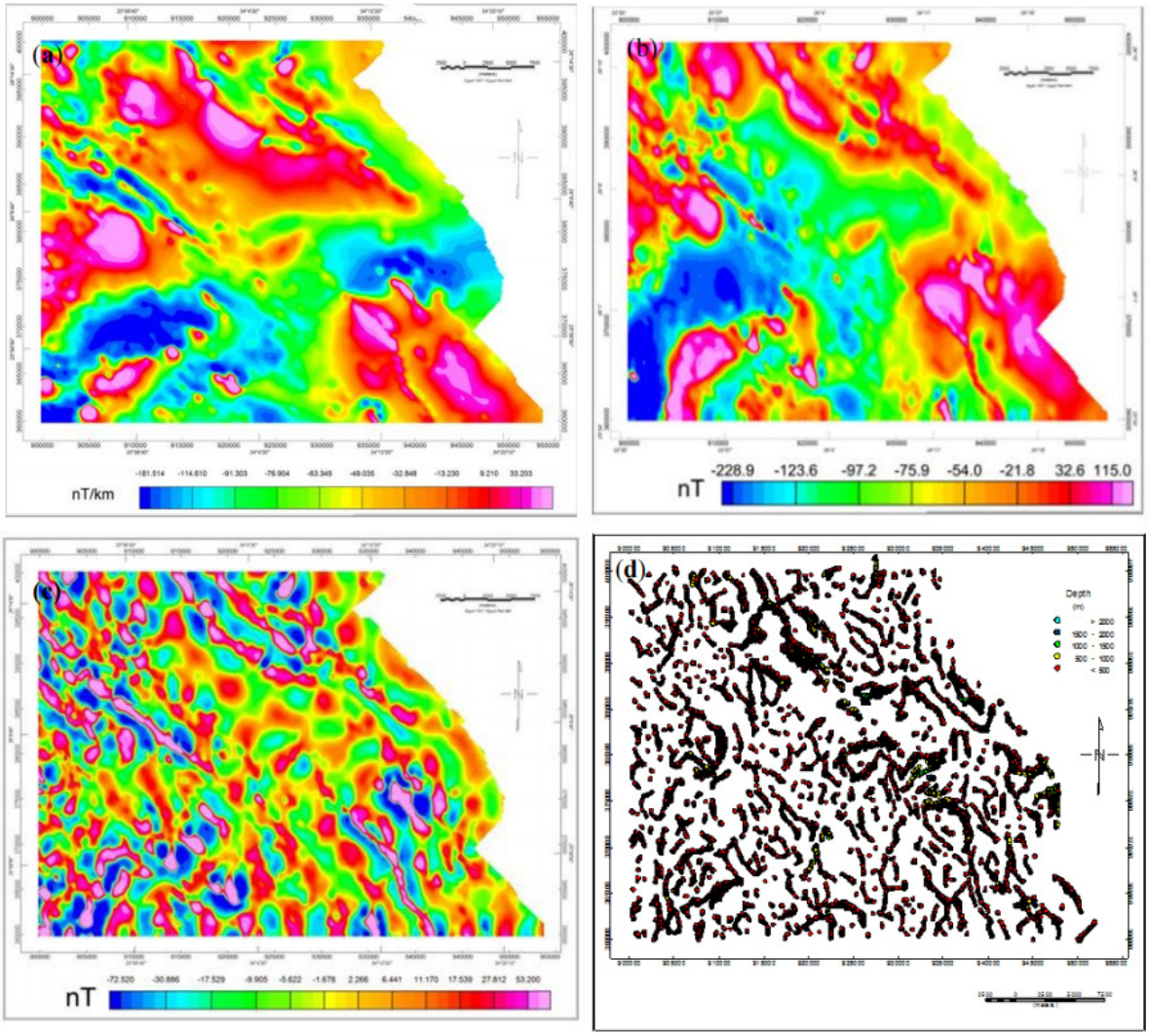

Figure 4. (a) Total magnetic intensity map of the study area; (b) reduction to the pole map of the study area; (c) residual magnetic anomaly map; (d) standard Euler deconvolution applied to RTP magnetic intensity map with structural index (SI) = 0.

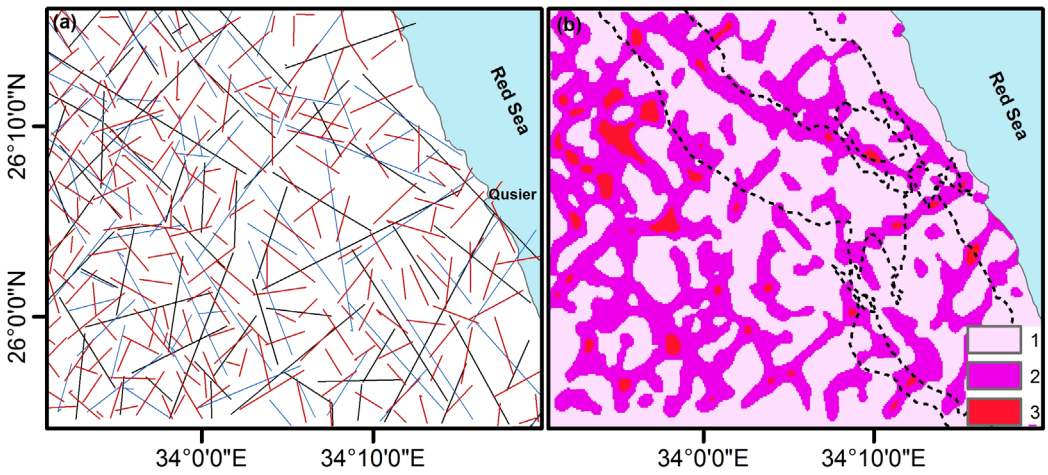

Figure 5. (a) Lineaments derived from magnetic anomaly maps; (b) lineament density map from magnetic maps revealing linear anomalies of deep seated structures of regional extent.

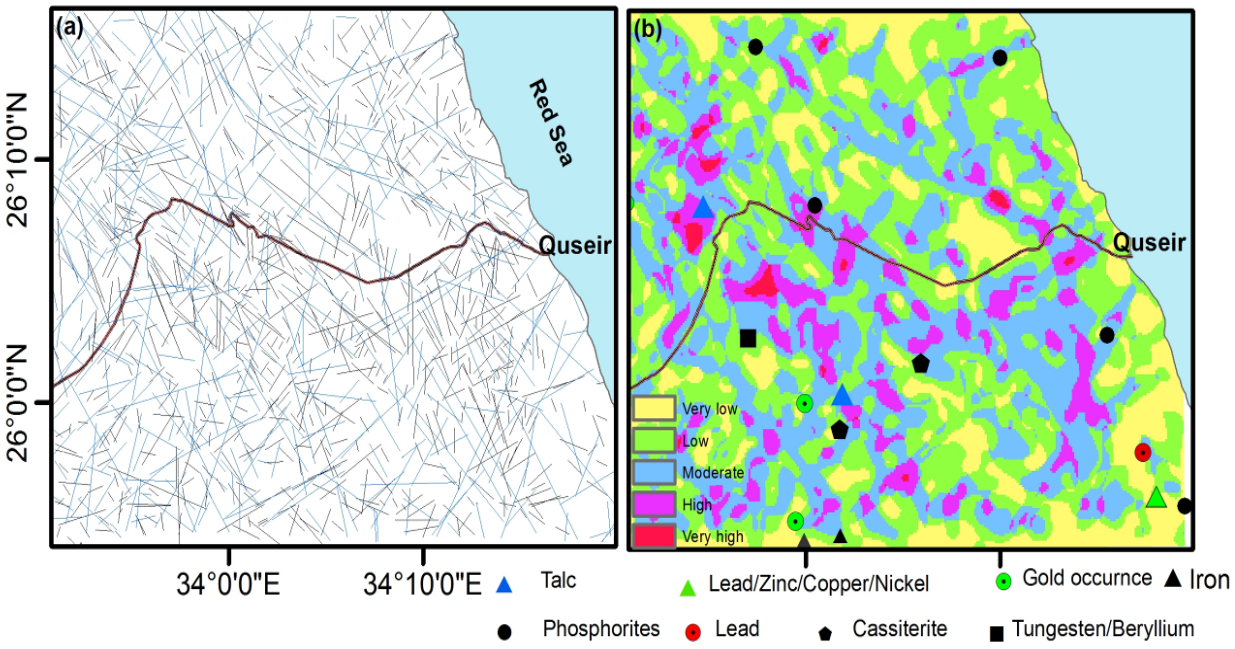

Figure 6. (a) An integrated lineaments from remote sensing (black) and magnetic data (blue); (b) lineament density map from remote sensing and magnetic data.

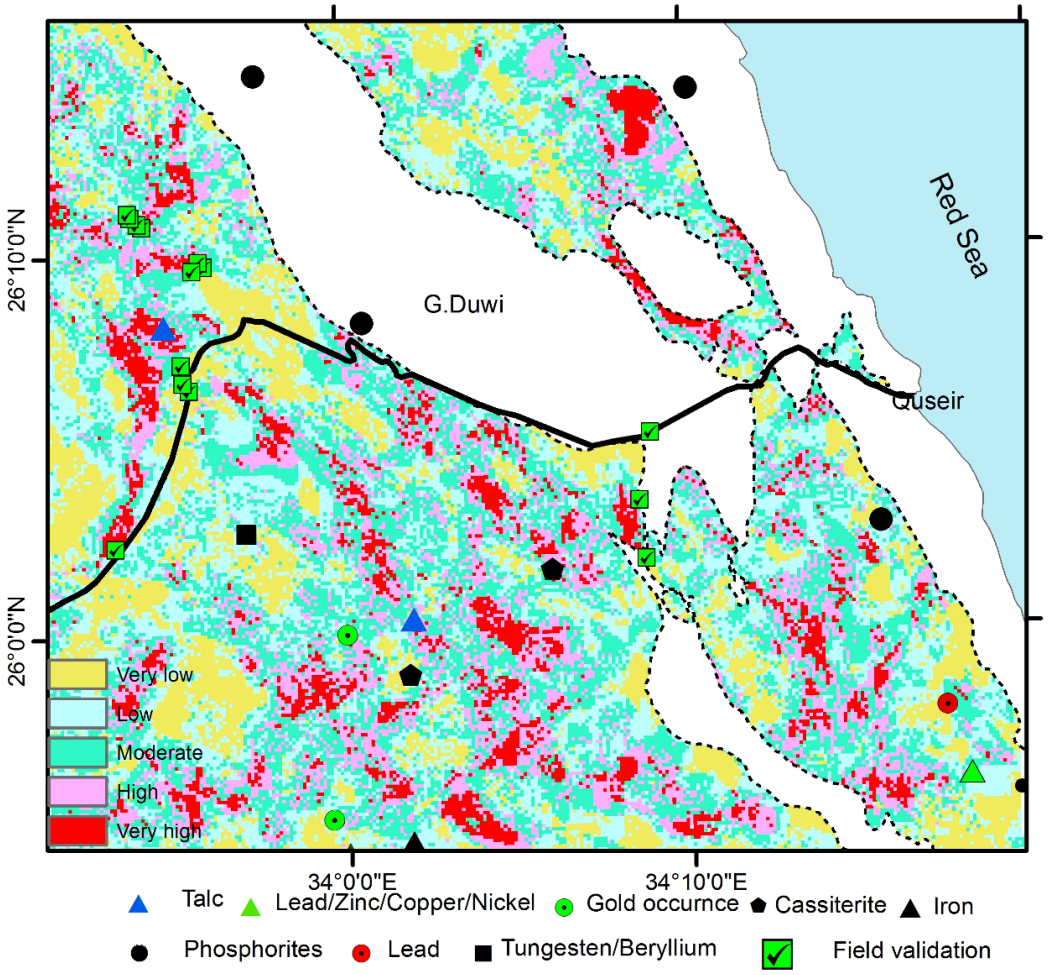

Figure 7. The mineral predictive map obtained by combining alteration zone and lineaments.

role in controlling the geodynamic evolution of the study area. Also it is shown that there are several strike slip faults were detected in NE-SW and NW-SE directions that have sub-surface continuation (**Figure 5a, Figure 5b**). This explains a probable dislocation of G. Duwi area north of Qift-Quseir Road from its counterpart of the sedimentary succession in the south. Landsat data validated these trends which controlled the rock units and also represent the favorable sites of the hydrothermal solutions.

In order to prepare the lineament map for further combination, we classified it into five classes after assigning weigh factors represented by numeric numbers 1, 2, and 3 (**Figure 6b**). The high value represents the higher density and the favorable site of mineral resources. Since several mineral deposits are related to hydrothermal solutions that ascending through fractures/fault zones. Therefore, zones of higher lineament density which related to tectonic/structural deformation of the lithosphere[31] represent a prone area of mineral resources. After converting the lineament density map into a weighted map, we superimposed the existing mines on this map. This results in **Figure 6b** revealed a positive correlation between the primary mineral-occurrences such as talc, iron, cassiterite, and Cu-Au-Pb-Zn mineralizations.

6. Integrated maps for predicting areas of mineral resources

The method of combining several data in a geospatial analysis technique is significant in mineral potential mapping[30]. To determine the probable area of mineral resources in the form of weighted map, an integrated approach has been adopted for characterizing the areas of mineral occurrences[42]. These data were adapted in raster to allow comparing and integrating peer-pixels in the image array. In this section, the lineaments and alternation zones that generated from RS and AMG data are integrated. They represent the appropriate indicators of mineralization and are effective reconnaissance approach in mineral exploration.

This process of hydrothermal activities commonly occurs along the faults and fracture zones. In addition, radar remote sensing data allowed detecting fracture and fault zones (lineaments). Thus, integration of optical and radar RS data can help in detecting mineral resources associated with hydrothermal solutions. Therefore, when considering the optimal location for a new mineral prospect, there are many factors need to be considered, including, for example, the fracture/fault zones and alteration zones.

Applying a spatial dimension of these factors using geographic information system (GIS) could be a useful tool to find the suitable location for new mineral prospect. Find the high lineament density area by applying spatial analysis technique allowed detecting the most area of fracture/fault zones. Such areas represent the favorable sites for mineral occurrences; therefore, we classified the lineament density map into several classes, the highest class represents in red color, while the lower represents in light magneta (**Figure 6b**).

The high areas of alteration appear with a red color, followed by magenta, cyan, and yellow colors. In order to achieve the optimal result, we combined the altered areas which obtained from multi-sources and the lineament density map. The results revealed that the most suitable areas predicted by GIS tool are consistent with areas of high alteration and high lineament density. Moreover, these areas display good correlation with the well-known area of the existing mines (**Figure 7**). These combined data from remote sensing including lineaments and alteration zones (**Figure 2g, Figure 6b**) can be employed in predicting areas of probable mineral resources.

6.1 Mineral predictive map

The collected data were digitally superimposed in a GIS and combined using spatial analysis techniques. The final map after combining lineaments (from aeromagnetic data, and remote sensing) magnetic residual anomalies, and HAZs allowed delineating the probable sites of mineral resources. This map was distinguished into five zones including very high, high, moderate, low, and very low areas of mineral occurrences. Overlay the existing sites of mineralization on the final map revealed that talc, cassiterite, gold, and copper/lead mineralization dis-

played positive correlation with areas of very high to high favorability (**Figure 7**). However, some mineralizations are difficult to be predicted that aren't correlated with lineaments or alteration zones such as phosphorites.

6.2 Field validation

In order to validate the extracted lineaments, predicted areas of alteration zones, and verify the mineral potential map, we have used existing mines and conducted field trip in November 2016. Based on field observations, the NW lineaments were predominant over the other trends. Most of these features include fractures/fault zones that are filled by quartz veins, sills, and dykes mostly of felsic composition (**Figure 8**). Five field stops were checked, most of these sites revealed minerals involved with hydrothermal activities such as talc, gold, and areas rich in muscovite and talc-schist. However, some areas were related to altered metavolcanics and associated metapyroclastics in the right hand of Qift-Quseir road. Some trends that were extracted from the aforementioned data are clearly observed in the field e.g. strike slip faults along the major trends of NW-SE, and some of them allowed formation of the sedimentery basins. These trends may control the rock units and mineralizations. They are mostly shears and fractures that vary from centimeters to meters in width, mostly occupied by quartz veins. Foliations and alterations are common in these rocks that represented by multi-deformation.

Evidences of alteration processes include multi-colored rocks, silicification, iron-oxides, and carbonization that varies in thickness. The host rocks of the metavolcanics were sheared and altered to talc-carbonates. It pervasively altered to carbonates and micaceous minerals. Field investigations revealed that the tested areas characterized by alteration zones enriched in talc, calcite and secondary amphiboles. It is found that the HAZs are more consistent with the lineaments extracted from the magnetic intensity map (**Figure 7** and **Figure 8**). This indicated that alteration zones usually connected to deep lineaments. This integration shows that the approaches of RS and AMG maps are effective techniques for exploring iron- and OH bearing minerals. Moreover, they presented a positive relationship between the primary mineral occurrences and areas of high lineaments and alteration zones.

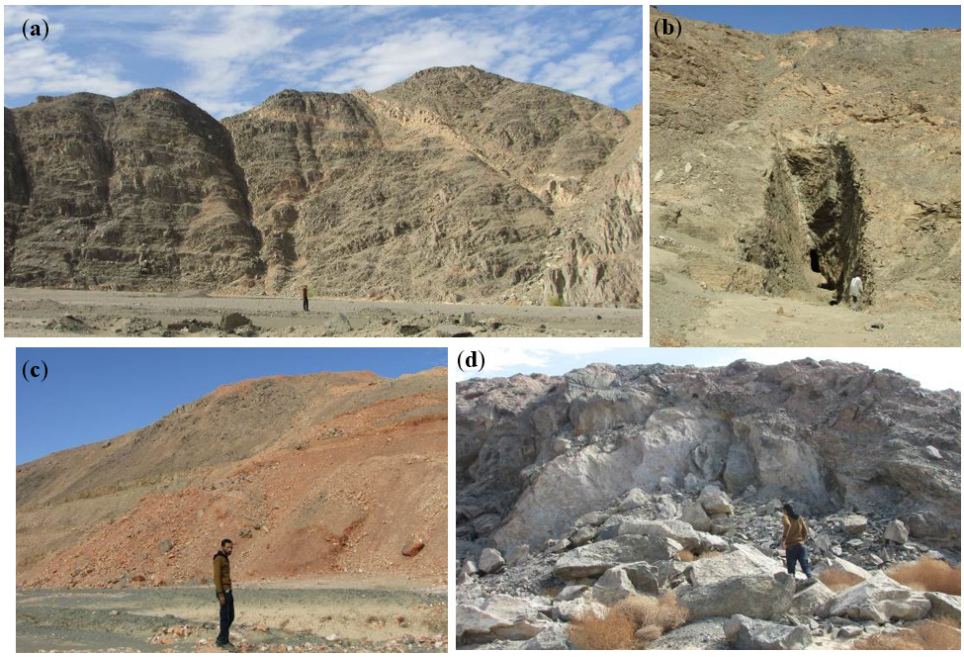

Figure 8. Field photographs (a) NW-SE joints, swarms of dykes and faults that cutting the metavolcanic rocks; (b) NW-SE quartz vein and alteration zones in gold mineralization; (c) site of hematite and quartz veins; (d) talc associated with serpentinites.

7. Conclusions

The study area is located west of the Quseir city, Red Sea, Egypt. Integration of RS and AMG data allowed detecting structural discontinuity and HAZs in the present study area. Image transformation techniques including band ratios and PCA were performed to Landsat OLI to reveal area of HAZs. The resulting image was discriminated into five zones characterizing the degree of the alteration. SRTM data was used to extract lineaments. Subsurface lineaments were delineated using the AMG data with several tools. In order to maximize area of probable mineral resources, HAZs and lineament density were combined to prepare the mineral prospect map. Field validation allowed verifying the prepared map and revealed several mineralized zones including talc, gold mines and quartz veins-bearing hematite.

Conflict of interest

The authors declare that they have no conflict of interest.

Acknowledgments

We thank the World Academy of Science (TWAS) for the support.

References

1. Sultan M, Arvidson RE, Sturchio NC. Mapping of serpentinites in the Eastern Desert of Egypt by using Landsat thematic mapper data. Journal of Geology 1986; 14(12): 995–999.
2. Abdelsalam MG, Stern RJ, Berhane WG. Mapping gossans in arid regions with Landsat TM and SIR-C images: The Beddaho Alteration Zone in northern Eritrea. Journal of African Earth Sciences 2000; 30(4): 903–916.
3. Madani A, Abdel Rahman EM, Fawzy KM, *et al.* Mapping of the hydrothermal alteration zones at Haimur Gold Mine Area, South Eastern Desert, Egypt using remote sensing techniques. The Egyptian Journal Remote Sensing Space Science 2003; 6: 47–60.
4. Ramadan TM, Kontny A. Mineralogical and structural characterization of alteration zones detected by orbital remote sensing at Shalate in District, South Eastern Desert, Egypt. Journal of African Earth Sciences 2004; 40: 89–99.
5. Abdelkareem M, El-Baz F. Characterizing hydrothermal alteration zones in Hamama area in the central Eastern Desert of Egypt by remotely sensed data. Journal of Geocarto International 2018; 33: 1307–1325.
6. Ahmed A, Abdelkareem M, Asran AM, *et al.* Geomorphic and lithologic characteristics of Wadi Feiran basin, Southern Sinai, Egypt, using remote sensing and field investigations. Earth System Science Journal 2017; 126(85): 1–25.
7. Abdelkareem M, El-Din GMK, Osman I. An integrated approach for mapping mineral resources in the Eastern Desert of Egypt. International Journal of Applied Earth Observation and Geoinformation 2018; 73: 682–696.
8. Sabins F. Remote sensing principles and interpretation. 3rd ed. W.H. Freeman Company; 1997. p. 494.
9. Sabins F. Remote sensing for mineral exploration. Ore Geology Review 1999; 14: 157–183.
10. El Khidir SO, Babikir IA. Digital image processing and geospatial analysis of landsat 7 ETM+ for mineral exploration, Abidiya area, North Sudan. International Journal of Geomatics and Geosciences 2013; 3(3): 645–658.
11. Amuda OS, Adebisi S, Jimoda L, *et al*. Challenges and possible panacea to the municipal solid wastes management in Nigeria. Journal of Sustainable Development Studies 2014; 6(1): 64–70.
12. Poormirzaee R, Oskouei MM. Use of spectral analysis for detection of alterations in ETM data, Yazd, Iran. Applied Geomatics Journal 2010; 4: 147–154.
13. El-Din GK, Abdelkareem M. Integration of remote sensing, geochemical and field data in the Qena-Safaga shear zone: Implications for structural evolution of the Eastern Desert, Egypt. Journal of African Earth Sciences 2018; 141: 179–193.
14. Abdelkareem M, El-Baz F. Mode of formation of the Nile Gorge in northern Egypt: A study by DEM-SRTM data and GIS analysis. Geological Journal 2015; 51: 760–778.
15. Goetz AFH, Rock BN, Rowan LC. Remote sensing for exploration, an overview. Economic Geology

1983; 78: 573–590.
16. Segal DB. Use of landsat multispectral scanner data for definition of limonitic exposures in heavily vegetated areas. Economic Geology 1983; 78: 711–722.
17. El-Etr HA, Yousef MSM, Dardir AA. Utilization of Landsat images and conventional aerial photographs in the delineation of some aspects of the geology of the Central Eastern Desert, Egypt. Annals of Geological Survey of Egypt 1979; 9: 136–162.
18. O'Connor EA, McDonald AJW. Application of remote sensing for geological mapping in Eastern Desert, Egypt. Proceeding of IGARSS' 88 symposium, Edimburg, Scotland; 1988. p. 631–632.
19. Sultan M, Arvidson RE, Duncan IJ, *et al.* Extension of the Najd shear system from Saudi Arabia to the Central Eastern Desert of Egypt based on integrated field and Landsat observations. Tectonics 1988; 7: 1291–1306.
20. El-Rakaiby ML. The use of enhanced Landsat-TM image in the characterization of uraniferous granite rocks in the central Eastern Desert, Egypt. International Journal of Remote sensing 1995; 16(6): 1063–1074.
21. Farghaly AMA. Structural framework of the Central-Eastern Desert of Egypt, using remote sensing techniques and ground data [PhD thesis]. Sohag: South Valley University; 1999.
22. Gad S, Kusky T. Lithological mapping in the Eastern Desert of Egypt, the Barramiya area, using Landsat thematic mapper (TM). Journal of African Earth Sciences 2006; 44(2): 196–202.
23. Sultan M, Arvidson RE, Sturchio NC, *et al.* Lithologic mapping in arid regions with Landsat thematic mapper data: Meatiq Dome, Egypt. GSA Bulletin 1987; 99(6): 748–762.
24. Conoco. Geological map of Egypt, scale 1:500,000, sheet NG 36 NW Quseir-NG 36 NW Asyut, Egypt. The Egyptian General Petroleum Corporation, Cairo, Egypt; 1987.
25. Said R. Tectonic framework of Egypt and its influence on distribution of Foraminifera. AAPG Bulletin 1962; 45: 198–218.
26. Said R (editor). The geology of Egypt. Rotterdam, Brookfield: A. A. Balkema; 1990.
27. Ghebreab W. Tectonics of the Red Sea region reassessed. Earth-Science Review 1998; 45: 1–44.
28. Gass IG. The evolution of the Pan African crystalline basement in NE Africa and Saudi Arabia. Journal of the Geological Society 1977; 134: 129–138.
29. Kröner A. Ophiolites and the evolution of tectonic boundaries in the Late Proterozoic Arabian-Nubian Shield of Northeastern Africa and Arabia. Precambrian Research 1985; 27(1-3): 277–300.
30. Rigol-Sanchez JP, Chica-Olma M, Abarca-Hernandez F. Artificial neutral networks as a tool for mineral potential mapping with GIS. International Journal of Remote Sensing 2003; 24(5): 1151–1156.
31. Alexander Io, Samuel OO, Esther CM, *et al.* Integrating Landsat-ETM and Aeromagnetic data for enhanced structural interpretation over Naragwata area, North-Central Nigeria. International Journal for Science and Engineering Research 2015; 6(9): 2229–5518.
32. Gerck E, Hurtak JJ. Laser remote sensing of forest and crops in genetic-rich tropical areas. International Archives of Photogrammetry and Remote Sensing 1992; 436–438.
33. Cappaccioni B, Vaselli O, Moretti E, *et al*. The origin of thermal water from the eastern flank of the Dead Rift Valley. Terra Nova 2003; 15(3): 145.
34. Hsu SK. Imaging magnetic sources using Euler's equation. Geophysical prospecting 2002; 50: 15–25.
35. Thompson DT. EULDPH: A new technique for making computer-assisted depth estimates from magnetic data. Geophysics 1982; 47: 31–37.
36. Reid AB, Allsop JM, Granser H, *et al.* Magnetic interpretation in three dimensions using Euler deconvolution. Geophysics 1990; 55: 80–91.
37. Ramadan TM, Abdelsalam MG, Stern RJ. Mapping gold-bearing massive sulfide deposits in the neoproterozoic Allaqi Suture, Southeast Egypt with Landsat TM and SIR-C/X SAR images. Photogrammetric Engineering & Remote Sensing 2001; 67(4): 491–497.
38. Ramadan TM, Sultan SA. Integration of Remote Sensing, Geological and Geophysical Data for the Identification of Massive Sulphide Zones at Wadi Allaqi Area, South Eastern Desert, Egypt. M.E.R.C. Ain Shams University Earth Science Series 2004; 18: 165–174.
39. Eldosouky AM, Abdelkareem M, Elkhateeb SO. Inte-

gration of remote sensing and aeromagnetic data for mapping structural features and hydrothermal alteration zones in Wadi Allaqi area, South Eastern Desert of Egypt. Journal of African Earth Sciences 2017; 130: 28–37.

40. Ramadan E, Feng X, Cheng Z. Satellite remote sensing for urban growth assessment in Shaoxing City, Zhejiang Province. Journal of Zhejiang University Science 2004; 5(9): 1095–1101.
41. Shahi H, Kamkar-Rouhani A. A GIS-based weights-of-evidence model for mineral potential mapping of hydrothermal gold deposits in Torbat-e-Heydarieh area. Journal of Mining & Environment 2004; 5(2): 79–89.
42. Woldai T, Pistocchi A, Master M. Validation and sensitivity analysis of a mineral potential model using favourability functions. Applied GIS 2006; 2(1): 19.